LAWRENCE
LIVERMORE
NATIONAL
LABORATORY

LLNL-PROC-664677

Development of a High Spatial Resolution Detectorfor at-Wavelength Metrology of X-Ray Optics

J. K. Vogel, H. B. Bhandari, J. Gaskin, S. R. Miller , V. V. Nagarkar, M. J. Pivovaroff, B. D. Ramsey, B. Singh

November 20, 2014

IEEE NSS MIC 2014
Seattle, WA, United States
November 8, 2014 through November 15, 2014

Disclaimer

Development of a High Spatial Resolution Detector for at-Wavelength Metrology of X-Ray Optics

Julia K. Vogel, Harish B. Bhandari, Jessica A. Gaskin, Stuart R. Miller, Vivek V. Nagarkar, Michael J. Pivovaroff, Brian D. Ramsey, Bipin Singh

***Abstract*—Recent advancements in the field of x-ray astronomy have relied significantly on innovations in grazing incidence x-ray optics technology, especially for the hard x-ray range for energies above 10 keV. The behavior of these x-ray telescopes for current and planned astrophysical and solar imaging missions needs to be well understood, and fully characterizing the optics includes measurement of the point spread function and effective area for flight optics as a function of energy and off-axis position as well as understanding the scattering and reflectivity properties of substrate coatings. This requires unique detectors with large areas, very high spatial resolution, high sensitivity, photon counting capability and energy discrimination. We report on the development of a detector that is well suited to meet these requirements. The key piece of the detector is a high spatial-resolution, electron-multiplying charge-coupled device. The detector is back-thinned and optically bonded via a fiberoptic taper to a purpose-fabricated high resolution, high brightness CsI:Tl scintillator with a microcolumnar structure. A prototype version of this camera was used to calibrate the x-ray focusing optics for the *Nuclear Spectroscopic Telescope Array* (*NuSTAR*) mission successfully operating in space since its launch in June 2012. Here we present our recent work on the design of the EMCCD detector and scintillators, fabrication, assembly and testing of the full detector system as well as our software development efforts for single photon detection and energy discrimination. Also included are first results from our recent measurement campaign at the x-ray stray light calibration facility at the NASA's Marshall Space Flight Center.**

I. Introduction

THE hard x-ray ($E \sim 10 - 100$ keV) Universe holds the key to answering many open questions in astronomy such as the physics behind black holes, supernovae explosions and compact objects. The technological advances in focusing x-ray optics over the last decade will help understand many of these long-standing mysteries. The advantage of focusing optics over previously employed devices like collimators and coded-mask cameras is their high sensitivity in the hard x-ray energy range above 10 keV. Sensitivities can be increased in this range by a factor of 100 using the novel technology over conventional devices. In recent years, such focusing optics equipped with multilayer-coated mirrors were developed for balloon payloads, such as the *High Energy Focusing Telescope* (emphHEFT, [1]) and form a vital part of current space missions such as the *Nuclear Spectroscopic Telescope Array* (*NuSTAR* [2]) and future observatories like *ASTRO-H* [3]. It is of crucial importance that the focusing components are well calibrated before being sent into space as well as once they are in orbit. To enable the full characterization of x-ray optics for current and planned astrophysical and solar imaging missions, including flight optics' measurement of the spatial resolution (point spread function, PSF) and the effective area (throughput of the telescope) as a function of energy as well as study of scattering and reflectivity properties of substrate coatings, we are developing a detector with:

- Very high spatial resolution (on the order of 25μm) through sub-pixel event localization,
- Minimized signal and resolution losses through deposition of microcolumnar CsI:Tl scintillator directly onto a fiberoptic (FO) taper,
- Wide dynamic range due to custom-made scintillators, for low- and high-energy measurements,
- Spectroscopic information and high detection efficiency over a wide x-ray energy range, from 5 keV ($\sim 100\%$) to over 100 keV (over 70%),
- Large active detector area ($\sim 5 \times 5$ cm^2) enabling optics calibrations to be performed with minimal scanning effort,
- High count-rate capability (order of 10^5 events/second depending on detector configuration) to use calibration time efficiently
- Design flexibility to accommodate the needs of various mission requirements,
- Simple, turn-key operation without need for cryogenics for easy operation.

II. The scintillator-coupled EMCCD detector

The central piece of the proposed detector is a high pixel-resolution, electron-multiplying charge-coupled device (EMCCD), back thinned and optically bonded to a specially fabricated high resolution, high brightness, microcolumnar CsI:Tl scintillator via a coherent fiberoptic taper. With this setup, x-rays incident on the scintillator-coupled EMCCD are converted into visible photons within the scintillator material and channeled towards the CCD chip without significant loss of spatial resolution. On the chip, the charges are collected, amplified and read out (see Figure 1).

Manuscript received November 15, 2014. We thank NASA for funding this research under SBIR grant number NNX12CA83C. Part of this work was performed under the auspices of the U.S. Department of Energy by Lawrence Livermore National Laboratory under Contract No. DE-AC52-07NA27344.

J. K. Vogel (e-mail: vogel@llnl.gov) and M. J. Pivovaroff are with Lawrence Livermore National Laboratory, Livermore, CA 94551, USA.

H. B. Bhandari, S. R. Miller, V. V. Nagarkar, and Bipin Singh are with Radiation Monitoring Devices (RMD) Inc., Watertown, MA 02472, USA.

J. A. Gaskin and B. D. Ramsey is with NASA Marshall Space Flight Center, Huntsville, AL, USA.

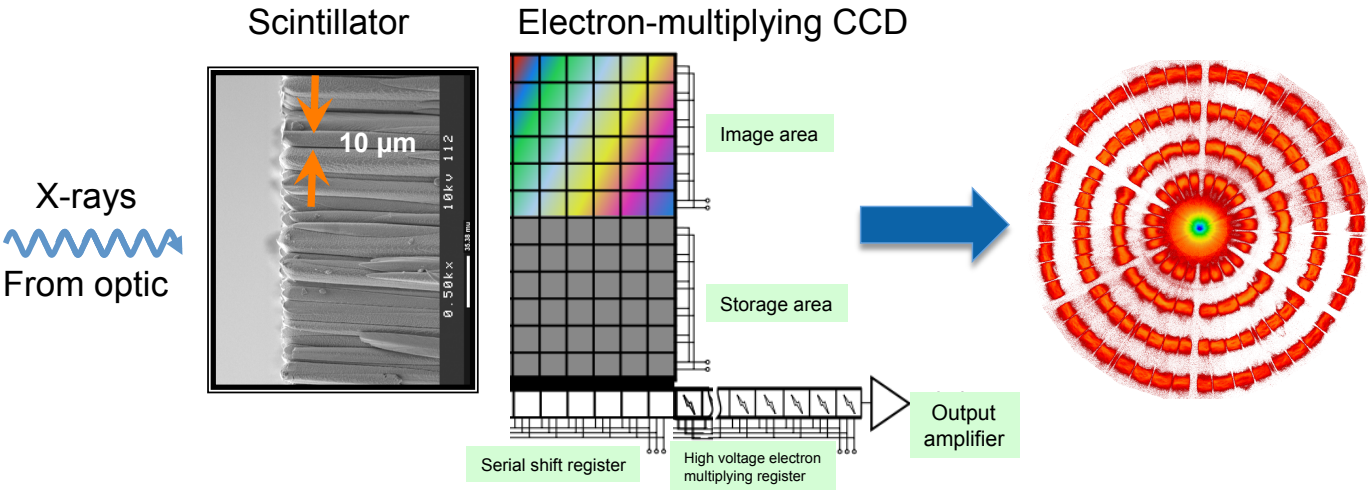

Fig. 1: Incoming x-rays are converted into visible photons within the microcolumnar-structured scintillator, which improves the spatial resolution as compared to conventional scintillator films. An EMCCD is then used to detect the photons and produce the image with maximal resolution and minimalized readout noise.

A. *Electron-multiplying CCD*

EMCCDs combine the high resolution and low noise features of a CCD with high internal gain and the very high sensitivity of an avalanche photodiode (APD). This is accomplished by placing a gain register after the shift register but before the output amplifier. The presence of internal gain allows high frame rates by effectively eliminating read noise, thus enabling individual x-ray photon counting.

The camera used for the prototype detector during Phase I of the project was an Andor iXon DV 887 EMCCD [4] with 512×512 pixels (16μm$\times 16\mu$m per pixel), permanently bonded to a $1:1$ fiberoptic window, with a specially designed $3:1$ fiberoptic taper that can be pressure-coupled to the CCD window of the EMCCD to achieve an effective imaging area of 24.5×24.5 mm^2 (see left part of Figure 2).

To improve the performance of the Phase I detector system and build on gained experience from detector feasibility measurements during *NuSTAR* optics calibration measurements at Columbia's Nevis Laboratories [5], an improved version of the Andor EMCCD was chosen as Phase II detector (Andor iXon DU 888, right part of Figure 2). This detector is back-illuminated, just like the Phase I detector, but has more pixels (1024×1024) of smaller size (13μm$\times 13\mu$m). It is also capable of handling higher frame rates at lower readout noise [6]. The most important specifications of this EMCCD are shown in Table I.

Before any experiments were conducted a series of calibration measurements were performed on the Phase II EMCCD detector testing and verifying especially single pixel readout noise and base level. The read noise was found to be in excellent agreement with the manufacturer's specifications and only one single pixel ([321, 547]) turned out to be damaged ("hot pixel"). It was excluded from the subsequent analysis. The base level is the average electronic DC offset for the dark and cooled ($-30°$C) detector at minimal exposure time and was determined to be around 400 counts, agreeing well with expectations.

B. *Structured scintillator*

Our structured scintillators consist of a high density, high light-yield, fast decay time, microcolumnar CsI:Tl film (see Figure 3) formed by vapor deposition. The high density and high average atomic number of CsI:Tl converts incident x-rays with high efficiency into visible light, and the microcolumnar structure channels the scintillation light by total internal reflection to the EMCCD via the taper. Furthermore, because of the microcolumnar structure, the scintillator structure can be made thick to absorb 10 keV to 100 keV x-rays with high efficiency without sacrificing spatial resolution, overcoming the traditional tradeoff between these two measures. Thus, a combination of the high stopping power and high light output of our microcolumnar CsI:Tl, along with its excellent light-channeling properties, will allow detection of x-rays with high efficiency, high signal-to-noise ratio (SNR, 4-19 depending on FO taper), and high spatial resolution. The strategy to enhance the detector sensitivity over the 8 to 100 keV x-ray energy

TABLE I: Specifications of the Phase II detector (Andor iXon DU 888).

Parameter	Specification
Pixel resolution	1024×1024
Pixel size	13 μm
EMCCD active area	13.3×13.3 mm^2
Pixel well depth	80,000 e$^-$
Gain register pixel well depth	240,000
Electron multiplier gain	1-1000
QE at 540 nm CsI:Tl light	95%
Operating temperature (OT)	TE-cooled to $-95°$
Dark noise at OT	$<<$ 1e$^-$/pixel/second
Read noise at 10 MHz readout	$<$ 1e$^-$ @ gain $= 40$

Fig. 2: Left: EMCCD camera (Andor iXon DV 887) with the permanently attached $1:1$ fiberoptic plug developed at RMD during Phase I of the project. A detachable $3:1$ fiberoptic taper is shown on the left. This system was used for integration and testing of the first scintillators [7], [8]. Right: Detector upgrade for Phase II. The new Andor iXon DV 888 provides a larger sensitive detector area with better spatial resolution through smaller pixel size. Top views of the new detector including the permanently bonded $1:1$ FO plug are shown in the top images, bottom images display the large (bottom left) and small end (bottom right) of the $3:1$ FO taper.

band is to use two separate scintillators; one for low energy x-rays (< 100 μm thick CsI:Tl) and the other for high energy measurements (> 400 μm thick CsI:Tl). The scintillator used with the detector is field-replaceable and this procedure does not require switching off the EMCCD, which reduces cooling time and therefore increases the operational efficiency.

Several approaches were followed in parallel to enhance the overall performance of the proposed structured scintillators:

1) Improved method of scintillator deposition: Thin films of CsI:Tl produced by vapor deposition commonly exhibit a columnar microstructure owing to cubic crystal structure of the material. Some of the parameters that influence the film structure are substrate temperature, deposition rate, angle of incidence and ambient vacuum. The effect of this structure on the scintillation properties of CsI is remarkable and hence its optimization based on its application is crucial. For the present application, the need for thick and uniform CMS CsI:Tl structures which exhibit a high degree of transparency and spatial resolution has been identified. Research and development efforts toward vapor deposition of thick CMS CsI:Tl scintillator structures were broadly made in three areas. These are upgrading the evaporator system, enhancing substrate preparation and patterning, and experimenting with deposition parameters that control the structure and chemical composition of the resulting film. An existing vapor deposition apparatus at RMD Inc. was upgraded to enable higher substrate temperatures via specially designed quartz halogen lamp heaters. Also low base pressure critical for synthesis of high-quality CsI:Tl structures with very negligible ($<$ 1 ppm) incorporation of impurities (residual gases) [9], [10] was enabled. Furthermore a planetary substrate holding system improves the homogeneity of the film deposition and provides an advantageous angle of incident for deposition.

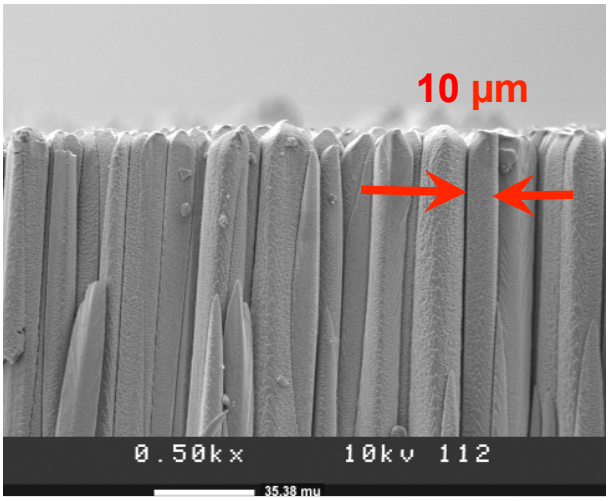

Fig. 3: Cross-sectional view of microcolumnar CsI:Tl film obtained with a scanning electron microscope (SEM). The film was deposited on a suitable substrate and the column diameter is about 10 μm on average.

Additional efforts were focused on directly depositing the scintillator onto the large end of the FO taper (as opposed to a standard substrate) and bonding the small end of the fiberoptic directly to the EMCCD. This minimizes the number and effects of optical interfaces between the scintillator and the EMCCD, thereby enhancing light coupling while minimizing resolution losses. While CsI:Tl was sucessfully deposited on a FO taper (see Figure 4) with good performance (column diameters from $<$ 1 μm to$\sim$ 20 μm), scintillators deposited

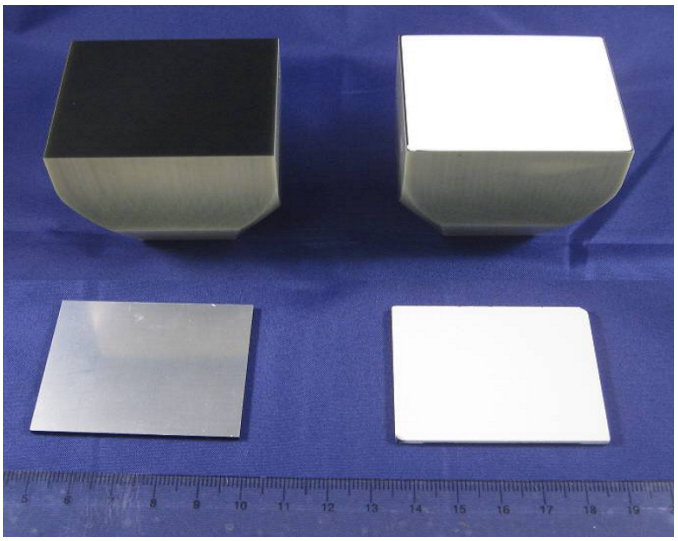

Fig. 4: The FO taper and substrates before and after scintillator deposition. The original FO taper is shown in the upper left, while the upper right taper has CsI:Tl directly deposited on it. A graphite substrate with aluminum reflective coating is shown in the lower part of the image before (left) and after CsI:Tl film deposition (right).

on graphite substrates allow for more experimental flexibility when the amount of light reaching the EMCCD through the scintillator can be increase via other methods such as the optimization of reflector material. This motivated the final choice of a dedicated low-energy and high-energy scintillator on graphite over a directly deposited scintillator on a FO taper.

2) Optimization of reflector material and protective layers: In the standard scintillator fabrication process, a layer of aluminum is typically used to coat the graphite substrates before deposition of the CsI:Tl film, in order to reflect the scintillation light that reaches the substrate end back toward the detector. Due to the nature of the substrate, such a coating shows reflectivity only on the order of 20%, although the reflectivity of Al (at normal incidence) is over 90% at the peak emission of CsI:Tl (540 nm). Improving the reflectivity is therefore one of the ways to enhance light collection. This is accomplished through substrate treatments prior to Al deposition and through exploring various reflective coatings created by RMD Inc.'s sibling company Evaporated Metal Films (EMF; Ithaca, NY). All these approaches improved reflectance, but the best combination was found to be the use of a glassy carbon substrate with a silver coating. Since the reflectance spectrum of silver is well matched with the spectral emission of CsI:Tl and comparable to that of aluminum over that range this does not come as a surprise. Figure 5 shows a comparison of the performance of a scintillator with Al and Ag reflector layer. The enhanced silver reflector material yields at least an increase of 30% in light output with no significant difference in the modulation transfer function (MTF) compared to the standard aluminum reflector. This indicates that the columnar growth of the CsI:Tl scintillator is not negatively influenced by the reflector surface. A comparison of MTFs for

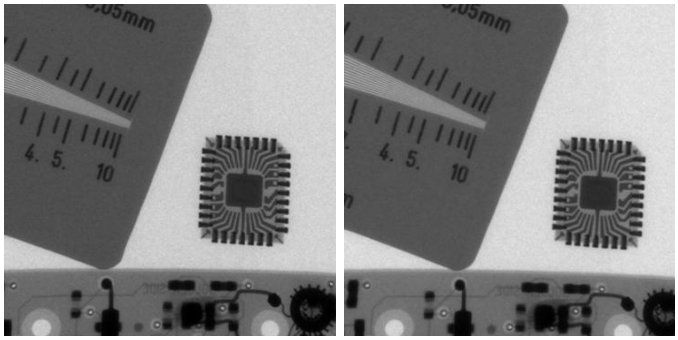

Fig. 5: Reflector comparison between aluminum and silver. Ag is about 30% brighter than aluminum, while yielding similar modulation transfer functions (MTFs). Left: Aluminum reflector. Protective layers of Parylene have been deposited between the graphite subtrate, the reflective Al coating and the CsI:Tl as well as on top of the scintillator material. Right: Silver reflector. The same protective layers were added as for the Al reflector.

various scintillators can be found in Figure 6. As a reference for light output and MTF a Kodak MinR film is included. Since the 150 μm thick RMD CsI:Tl scintillator is optimized for high x-ray absorption efficiency, the 70 μm thick MinR film appears superior. The numbers for the light output have been included in the plot as well and show that the aluminum- and silver-backed CsI:Tl films are brigther than the MinR film by a factor 4 (for Al) to 5 (for Ag). These performance improvements are significant and contributed to the sensitivity enhancements during Phase II.

Another improvement in addition to the reflectors is the hermetic sealing of hygroscopic films such as CsI:Tl using protective coatings. Parylene-C is an organic polymere that provides a protective barrier against moisture and has been applied to all scintillator film as transparent and blemish-free.

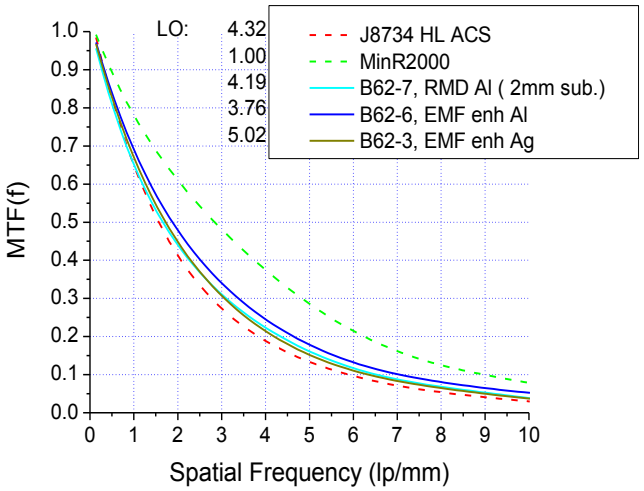

Fig. 6: MTFs of various scintillators deposited on different reflector material-coated substrates. Using silver reflective layers improves the light output by at least 30% as compared to Al reflectors without degrading the MTF.

3) Alternative deposition approach: While for standard radiography applications CsI:Tl is deposited in the form of amorphous microcolumnar scintillators (AMS), crystalline microcolumnar scintillator (CMS) CsI:Tl was also studied (see Figure 7). The goal is to minimize self-absorption while conserving high spatial resolution especially for thick scintillators. By changing deposition parameters, e.g. temperature, and using substrates with intrinsic patterns CMS can be grown exhibiting well-defined columns to channel the light and keep it from spreading. While the brightness of the CMS films is surperior, the columns are wider than in the case of AMS films (10 μm) resulting in a degradation of spatial resolution ($1-3$ lp/mm). Depending on the specifics of the application either AMS or CMS films can be useful.

4) Alternate scintillator materials: While CsI:Tl remains the material of choice due to its excellent scintillation properties and maturity of its deposition technology used to fabricate high resolution microcolumnar structures, other composition have been considered as well, such as Europium-doped Barium Cesium Iodide Ba_2CsI_5:Eu [11], a scintillation material that has demonstrated an extreme light yield of $97,000$ photons/MeV ($62,000$ ph/MeV for CsI:Tl), high density of 5.06 g/cm^3 (4.51 g/cm^3 for CsI:Tl) and negligible afterglow. The first step was to develop a cost-efficient and precise procedure to deposit the Ba_2CsI_5:Eu films. This was accomplished using low cost, commercial grade BaI_5, CsI, and EuI_2 to synthesize the scintillator material at the desired thickness with a microcolumnar structure. After optimizing the deposition parameters the same optimizations as for CsI:Tl were included in the scintillator manufacturing process, such as the use of reflector-coated graphite substrates and parylene protection. First results yield a spatial resolution of 6 lp/mm (at 10% MTF). Light output measurements for a 50 μm thick Ba_2CsI_5:Eu film indicate a gain of almost a factor of 4 compared to commercially available Gd_2O_2S (GOS) screens (MinR-2000, 34 mg/cm^2). Annealing the scintillator improved this result by another 11% by removing defects in the film and non-uniformities in the dopant distribution as well as improving the microcolumnar structure. Therefore Ba_2CsI_5:Eu can be a valid alternative to CsI:Tl. The overall specifications of the complete detector system combining the above outlined scintillators and EMCCD detector are summarized in Table II.

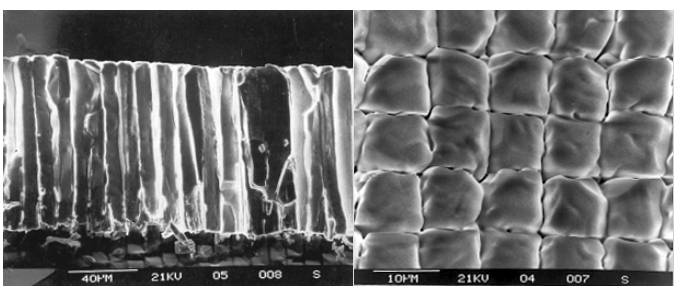

Fig. 7: SEM images of a CMS CsI:Tl film (left: side view, right: top view). While the columns are wider than in the AMS configuration, they are tightly packed yielding a transparent film.

TABLE II: Specifications of the high spatial resolution scintillator-coupled EMCCD

Parameter	Specification
EMCCD pixel resolution	1024×1024
EMCCD pixel size	13 μm
Scintillator-EMCCD coupling	Via $3:1$ coherent fiberoptic
Detector active area	39×39 mm^2
Intrinsic system resolution	39×39 μm^2
Frame rate	10 fps (full frame) to >500 fps (binning)
Low x-ray energy scintillator	<100 μm thick microcolumnar CsI:Tl
High x-ray energy scintillator	>400 μm thick microcolumnar CsI:Tl

III. Software Development

In addition to the enhancements on the hardware side, we also developed algorithms to detect single photon events based on background-subtracted test data acquired with radioactive sources. Each data set consists typically of multiple frames and noise can be suppressed by smoothing the data with a band pass filter prior to determining event locations on the chip, which increases the tracking efficiency of the events. The characteristic length scale of typical source events is taken into account to distinguish these events from *false* events resulting from noise or background variations still present in the data after the band pass filtering. We determined several cuts to be applied to the raw data including cuts on the event brightness, eccentricity of the features and their radius of gyration. The brightness cut, for example, takes into account that higher energy events appear brighter than low energy events which allows to cut remaining noise at low brightness. Typical events are only slightly elongated and generally circular restricting the eccentricity to small values (circular events have eccentricity zero, very elongated events show values of 1). The radius of gyration represents the root-mean-square distance of pixels from the center of gravity with the brightness of a pixel corresponding to the mass in our case and can be used to estimate the extent of a photon event. Figure 8 illustrates how the single photon counting algorithm works: a frame of raw data acquired with a ^{57}Co source is shown in the left panel. Background has been subtracted and around 12 events are expected in this particular data frame. The middle panel shows the result of our analysis with 16 events detected and displayed on the background-subtracted, smoothed original data set. Two of the applied cuts are indicated in the right panel of the same Figure, i.e. the most efficient cut in separating noise from data, which is the brightness cut shown in blue, and a cut on the extension of the event signatures (radius of gyration, red lines).

IV. Measurements with Phase I and II detectors

During the detector development, data were acquired for calibration and analysis purposes during Phase I and II and the performance of the final detector setup was verified with a concluding data taking campaign. More specifically, the detector prototype of Phase I was used for the calibration of the x-ray focusing optics of the Nuclear Spectroscopic Telescope Array (*NuSTAR*) at the Rainwater Memorial Calibration Facility (RaMCaF [5]) of Columbia University's Nevis Laboratories in Tarrytown, NY. Further detector calibration

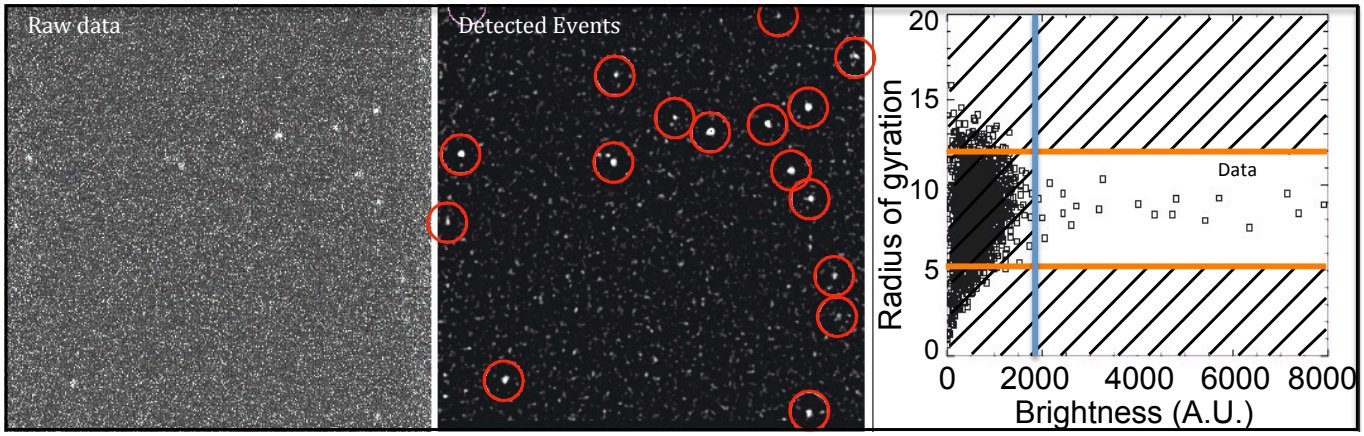

Fig. 8: Left: Typical frame of raw data after background subtraction. In this case data was acquired with ^{57}Co using a $3:1$ fiberoptic taper. Center: Detected events in the same frame after all cuts, superimposed on smoothed and passband-filtered data. Right: Typical cuts applied to the data for brightness and event extension.

data was acquired during Phase II at RMD Inc. (Watertown, MA) with several radioactive sources. The final measurements were conducted at NASA's Marshall Space Flight Center (MSFC) and the National Space Science Technology Center (NSSTC) in Huntsville, AL using HERO flight optics as well as radioactive sources together with the detector system in its final configuration.

A. *NuSTAR flight optics calibration*

NuSTAR is a NASA Small Explorer (SMEX) mission that was successfully launched in June 2012 and is led by PI Fiona Harrison of Caltech. This observatory is the first hard x-ray focusing telescope in space with sensitivity in the energy range of $3-79$ keV [2]. The instrument consists of two co-aligned focusing optics [12] with advanced CdZnTe detectors in the focal plane [13]. The scintillator-coupled EMCCD prototype played a crucial role during the *NuSTAR* on-ground calibration campaign and was used during the installation and alignment of the *NuSTAR* flight optics at RaMCaF. Work included the characterization of the point-spread function on-axis and off-axis, the validation of ray-trace simulations (see Figure 9), and the study of RaMCaF features in the experimental setup. Further details on these measurements and their analysis can be found in Reference [8].

B. *Calibration at RMD*

To support the development of the Phase II scintillator-coupled EMCCD, we acquired data with the detector using radioactive sources (^{241}Am, ^{57}Co, ^{109}Cd) that were characterized with a Germanium detector at RMD Inc.. These data sets, taken at various source-detector distances ($5-35$ inches) with three different scintillator materials, feed into the single photon counting (SPC) algorithm development and are used to tune and optimize the centroid-finding algorithms localizing the position of each detected x-ray photon. The specific scintillators tested were a 164μm thick CMS CsI:Tl film, a 1.65 mm CsI:Tl on BeO scintillator, and a CF-27 + PAgP (2×2, 400 μm thick) film. FO tapers were included in all the measurements.

The source spectra (background-subtracted and measured with a Ge detector) for ^{241}Am, ^{57}Co, and ^{109}Cd can be found in Figure 10. The peaks above 20 keV were used to characterize the scintillator-coupled EMCCD. Additional lines at lower energies are present for the ^{241}Am and ^{109}Cd sources (intrinsically shielded for the ^{57}Co source). These prooved useful to determine the low energy threshold of our EMCCD prototype, but complicated the tuning of our SPC algorithms since events of different energies, i.e. with various spatial extensions, brightness, etc., needed to be traced simultaneously.

After applying all cuts and scanning the frames for qualifying events as described above, we determined the number of detected photons and compared it to the number of expected counts as obtained from the source calibration measurements using the Germanium detector. Cuts were improved iteratively on a subset of the data until good agreement between data and expectation was achieved. Then the algorithms were tested on the remaining data for a specific setting. We verified that the peaks in the spectra remained at the same energy value for various detector-source distances d and the count rate

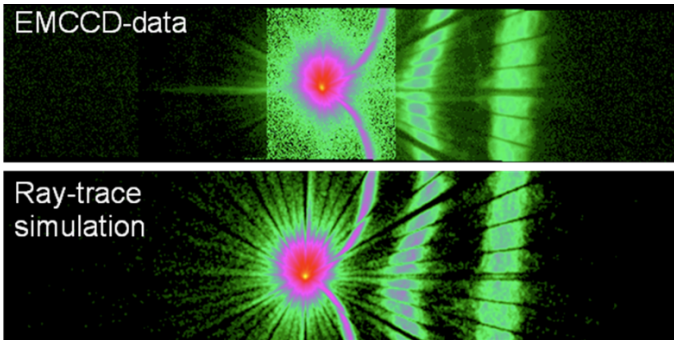

Fig. 9: Comparison between data acquired at RaMCaF for one of the *NuSTAR* optics with the EMCCD Phase I prototype detector and results of ray-trace simulations. The x-ray source is located 8 arcminutes off-axis in this case and data and simulation agree well.

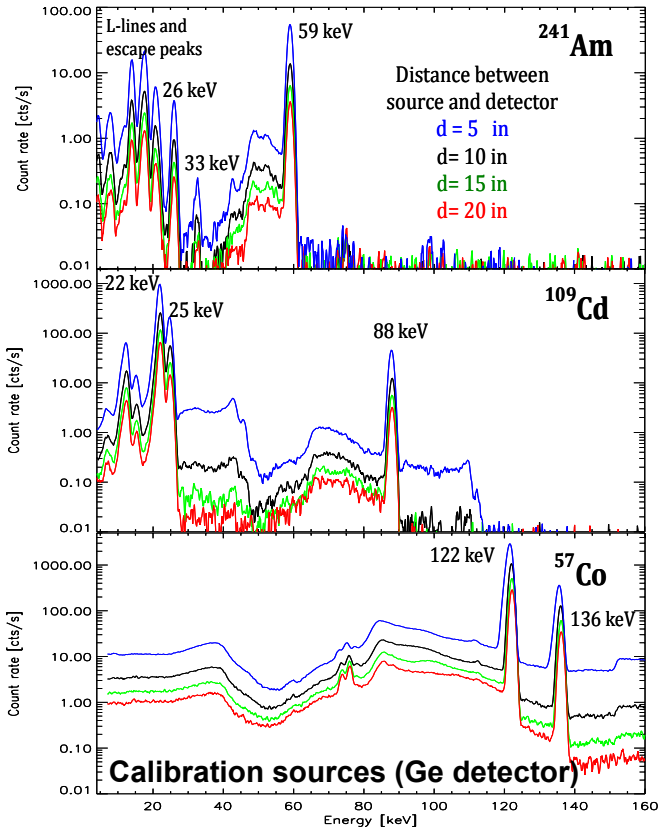

Fig. 10: Spectra of the calibration sources for the scintillator-coupled EMCCD: ^{241}Am (top panel), ^{109}Cd (middle panel) and ^{57}Co (bottom panel) for various distances between source and detector.

exhibited the expected $1/d^2$-dependence (see Figure 11). This establishes that the observed events are clearly originating from the source. Work to determine the final energy resolution is currently ongoing.

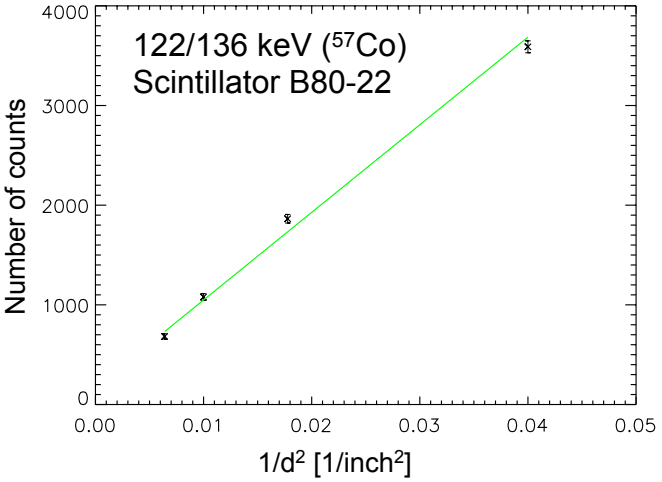

Fig. 11: Linear relation between number of counts and $1/d^2$ in observed 122/136 keV line of ^{57}Co. Data obtained with a CF-27 + PAgP (2×2, 400 μm) scintillator is shown.

C. Flight optic measurements at MSFC

Measurements employing the scintillator-coupled EMCCD detector in its final configuration were conducted at the Stray Light Facility (SLF) at NASA MSFC and the X-Ray Laboratory (XRL) at the NSSTC in Summer 2014.

At the 100 m long MSFC SLF (see Figure 12) the detector was used to capture the image of the HERO/HEROES (High Energy Replicated Optics/High Energy Replicated Optics to Explore the Sun [14], [15]) telescope (see small image in Fig. 12). Various energies ($15 - 40$ keV) and intensities were measured after aligning the optic and determining the best-focus position for the detector. From the data acquired in this configuration, the point-spread function of the optics was measured (see Figure 13) and the half power diameter (HPD) was determined. The results indicate an HPD of about twice the known HERO HPD of $26''$. The reason for the higher than expected HPD is most likely a combination of several factors: the detector was not exactly positioned at best-focus, an off-axis PSF rather than the on-axis PSF was observed and the estimation of the 100% encircled flux over-estimates the real value, e.g. due to noise or the fact that not the full flux is captured. No significant energy dependence was observed for the HPD.

Further data were acquired at NSSTC's XRL for two scintillators with different radioactive sources to cover the energy range from $8 - 60$ keV. One of the sources was a multi-energy selectable ^{241}Am source, the other a high-intensity ^{241}Am probe. The multi-energy selectable source provides the following filters/energies: Cu ($K_\alpha = 8.0$ keV), Rb ($K_\alpha = 13.4$ keV), Mo ($K_\alpha = 17.4$ keV), Ag ($K_\alpha = 22.1$ keV), Ba ($K_\alpha = 32.2$ keV), and Tb ($K_\alpha = 44.5$ keV). Data were acquired for both two scintillators and Figure 14 shows an example of a typical set of data. In this case, the Cu filter was used (8 keV) with a 1.65 mm CsI:Tl on BeO scintillator and the $3:1$ fiberoptic taper. Intensities were normalized to 1. Figure 15 shows the cross section along the black line

Fig. 12: Image of the about 90 m long connection tunnel between the source room and the instrument/detector cleanroom of the Stray Light Facility at MSFC. The total length of the facility is 100 m.

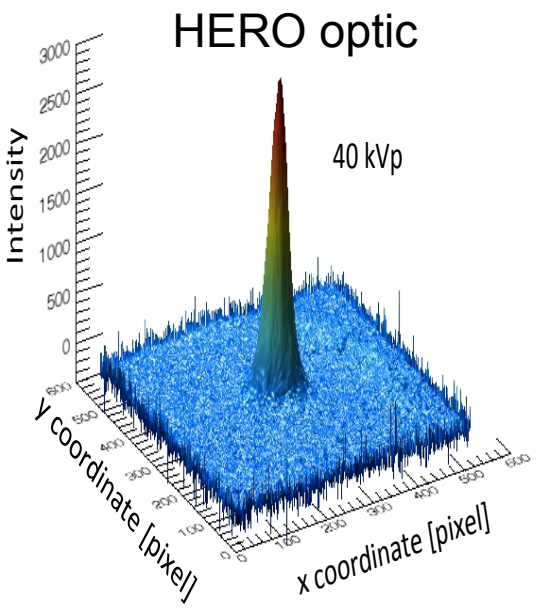

Fig. 13: 3-d intensity image of the HERO telescope acquired 40 kVp using a 1.65 mm CsI:Tl on BeO scintillator. These data were used to estimate the HPD of the optics.

indicated in Figure 14, i.e. a cross-section along the center of the intensity peak at $x = 540$. In addition to the Cu data, images acquired in the same manner for the Ag, Tb and Am data with the same scintillator are displayed. Normalized data are represented as symbols, while the lines indicate Gaussian fits to the data. Due to lower statistics, the lower energy data exhibit some fluctuations. As can be seen, photon energies down to 8 keV can be clearly detected (in integration mode), providing an upper limit on the low-energy threshold (8 keV

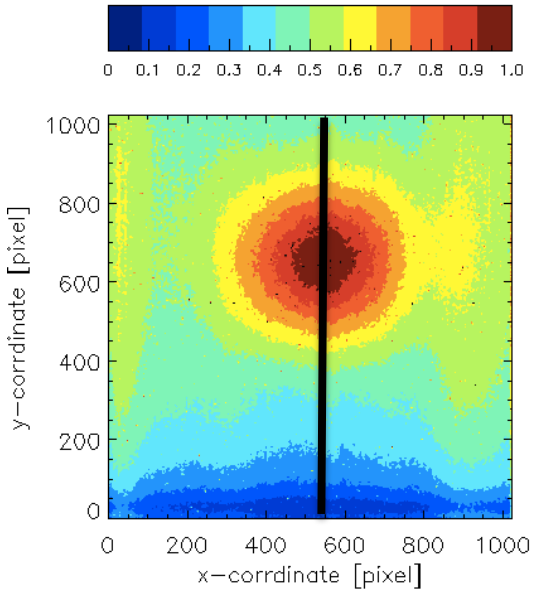

Fig. 14: Normalized Cu (8 keV) data acquired at NSSTC's XRL using a 1.65 mm CsI:Tl on BeO scintillator.

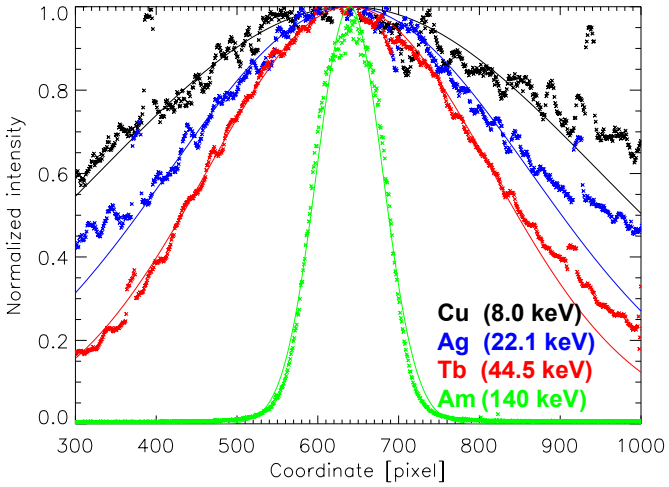

Fig. 15: Cross-section along x=580 pixel (as indicated by black line in Figure 14). Additionally, higher energy data was included.

was the lowest energy at which data were acquired at the NSSTC). It is also observable that the peaks get narrower with higher energies. If single photon counting can be applied for all energies, which is still work in progress for these data, each peak should get narrower.
More data sets were acquired at MSFC and NSSTC and analysis is still ongoing.

V. Conclusion

In this contribution, we present results of the development and construction of a high-spatial resolution detector for calibrating hard x-ray telescopes. We report on hardware upgrade such as the scintillating materials and their deposition. Furthermore, we show advances on the software side made by developing algorithms to detect single photon events. Currently we are finalizing the analysis of data acquired with the detector system in its final configuration at NASA MSFC and NSSTC and are preparing the scintillator-coupled EMCCD for delievery to our sponsor.

Acknowledgment

Part of this work was performed under the auspices of the U.S. Department of Energy by Lawrence Livermore National Laboratory under Contract DE-AC52-07NA27344. We thank NASA for funding this research under grant number NNX12CA83C.

References

[1] F. A. Harrison et al., Exp. Astron., 20,131-137 (2005).
[2] F. A. Harrison et al., ApJ, 770, 103 (2013).
[3] H. Kunieda et al., Proc. SPIE Int. Soc. Opt. Eng. 7732, 773214 (2010).
[4] http://occult.mit.edu/_graphics/poets/info/ixon_dv887bi.pdf
[5] N. F. Brejnholt et al., X-Ray Optics and Instrumentation, 2011, 285079 (2011).
[6] http://www.andor.com/pdfs/specifications/Andor_iXon_888_Specifications.pdf.
[7] H. Kudrolli et al., JINST, 6, C12013 (2011).
[8] J. K. Vogel et al., Proc. SPIE Int. Soc. Opt. Eng. 8443, 84432L , (2012).
[9] K. Okamoto et al., Thin Solid Films, 147, 3, 16 (1987).

[10] H. L. Caswell, Hollis L., Journal of Applied Physics, 32, no.1, pp.105,114 (1961).
[11] E. D. Bourret-Courchesne et al., Nucl. Instr. Meth. A, 612, 138 (2009).
[12] C. J. Hailey et al., Proc. SPIE, 7732, 77320T (2010).
[13] F. A. Harrison, W. R. Cook, H. Miyasaka, & R. McLean, in Semiconductor Radiation Detection Systems, ed. K. Iniewsk (Boca Raton, FL: CRC Press), 67 (2010).
[14] B. D. Ramsey et al., Proc. SPIE Int. Soc. Opt. Eng., 4138, 147 (2000).
[15] S. D. Christe et al., Proc. SPIE Int. Soc. Opt. Eng., 8862, 886206 (2013).